12-2013

# STIMULATED RAMAN SCATTERING IN MICRO SPHERE RESONATORS

Ruoyu Zhang
*Clemson University*, zhang.ruoyu.1988@gmail.com

**STIMULATED RAMAN SCATTERING IN MICRO SPHERE RESONATORS**

---

A Thesis
Presented to
the Graduate School of
Clemson University

---

In Partial Fulfillment
of the Requirements for the Degree
Master of Science
Electrical Engineering

---

by
Ruoyu Zhang
December 2013

---

Accepted by:
Dr. Lin Zhu, Committee Chair
Dr. Eric G. Johnson
Dr. Liang Dong

**ABSTRACT**

Micro sphere resonators that hold optical whisper gallery modes (WGMs) provide an innovative option for implementing micro optical resonators. The unique properties of the micro sphere resonator make it capable to introduce resonance for various optical phenomenon, like stimulated Raman scattering (SRS), in micron scale.

This thesis illustrates the characteristics of micro sphere resonators and demonstrates the resonance-enhanced SRS in micro sphere resonators with reduce threshold power. Both theoretical and experimental results are presented. Coupling model for WGM is derived in transfer matrix method. Simulation analyses for mode pattern of WGMs are solved based on mathematic model and finite element method (FEM). Fabrication of devices like silica binocular tapered fiber couplers and silica micro spheres is developed. The measurement setup is established, based on which characteristics of silica micro sphere resonators are measured. The result is compared to theoretical analysis to obtain the Q-factor of the resonator. The correspondence of the Q-factor on the coupling condition and the degradation of the Q factor over time are further discussed. SRS in silica micro sphere resonators is demonstrated with a reduced threshold power as low as $1\ mW$, which is 2 to 3 orders lower than that in fiber-based devices. Fabrication and measurement on chalcogenide glass micro sphere resonators are presented, according to which the threshold for SRS is also calculated. Further work is needed to improve the Q-factor of the chalcogenide glass micro sphere resonator for demonstrating the resonance-enhanced SRS in this material.

**ACKNOWLEDGMENTS**

First and foremost, I would like to dedicate my sincere gratitude to my advisor, Dr. Lin Zhu, for his inspirational guidance during my study in Clemson University. The knowledge and insight in photonics and opto-electronics of Dr Zhu motivated me deeply in my research, and I would have never been able to complete this thesis without his encouragement, patience and support.

I would also like to thank Dr. Eric G. Johnson and Dr. Liang Dong for being my committee members. Through course works and research, their professional knowledge and attitude deeply impressed me and strengthened my background in optics.

I'm grateful and fortunate to have all my colleagues and friends in Clemson. I would like to express my appreciation to all members in my group, Chenguang Huang, Jiahua Fan and Yunsong Zhao, for being helpful workmates in research and generous friends in life. My appreciation also goes to Yuan Li, Indumathi Raghu, Aaron Pung, and Guancheng Gu for all the collaborations, the fun time, and the struggling nights on deadlines that we've shared.

Finally, I would like to thank my parents for their continued support and unconditional love, which is the source of encouragement of mine all through my life.

**TABLE OF CONTENTS**

Page

Table of Contents (Continued)

Page

## LIST OF FIGURES

List of Figures (Continued)

Figure Page

# CHAPTER ONE

# INTRODUCTION

## 1.1 Whisper Gallery Modes and Micro Sphere Resonators

Whisper gallery mode (WGM) is a type of mode propagating at the concave surface of spherical structures. It is first discovered as an acoustic phenomenon. The whisper uttered near the inside surface of a dome or spherical wall of the building could be heard only at other positions near the wall due to the propagation of acoustic waves along the concave structure. This unique property is the origin of the name "whisper gallery" [1].

Similar phenomenon also exists in optics, which draws lots of attentions recently and has been intensively investigated [2-8]. When light wave propagates at the concave surface of dielectrics with proper incident angles, the field will be confined in circulating modes near the surface due to the total internal reflection. This type of mode can be held by micro structures like micro spheres, rings and disks, providing a solution of novel optical resonators. Micro resonators with high quality factor (Q-factor) and small mode volume can trap the light in several tens of microns while maintain a long photon lifetime, enabling the reduction in size of resonance related optical devices like optical filters and lasers, and the integration of high Q resonators in micro optic circuits.

## 1.2 Stimulated Raman Scattering

For the scattering between photons and particles like atoms or molecules, most photons are scattered by changing the propagation direction with the same energy level as incident photons. In other words, there's no energy exchange between photons and particles during the scattering process, and thus the scattering is elastic, which is referred as Rayleigh scattering. However, energy exchange may happen to a small portion of photons. As a result, the atom or the molecule is excited to a different energy level, giving a scattered photon with frequency higher or lower than the incident one.

Raman scattering is the inelastic scattering of a photon with an atom or molecule. It was first discovered by C.V. Raman and K. S. Krishnan when observing the "weak second radiation" from liquid media [9]. The interaction of photons and atoms/molecules is illustrated by Figure 1.2.1. Since the energy could be transferred either from the photon to the atom/molecule, or from the atom/molecule to the photon, there are two possible situations for Raman scattering. When atoms/molecules receive energy and emit scattered photons with lower frequency, it is noted as Stokes Raman scattering. And for the situation when scattered photons have higher frequency than incident ones, it is noted as anti-Stokes Raman scattering [10, 11].

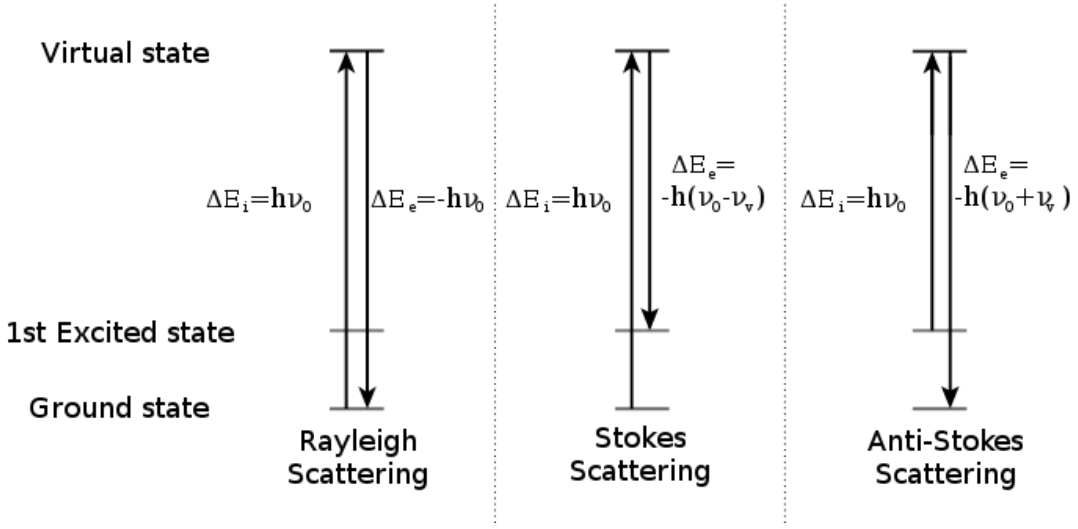


**Figure 1.2.1: Raman scattering process in energy level expression.**

The Raman spectrum shows the relative intensity of scattered light as a function to the frequency deviation from the incident light. Stokes and anti-Stokes scattering appear to be two symmetric patterns in shape with the same frequency deviation from the incident light frequency. The symmetry comes from the same energy difference between twos specific states. However, intensities of the two patterns are usually different due to the difference population states in upper and lower levels. Since the upper level is less populated than the lower level, Stokes scattering is usually stronger than anti-Stokes scattering. The strength of each kind of scattering depends on the temperature.

Besides spontaneous Raman scattering, there's also stimulated Raman scattering (SRS). If some Stokes photons are injected to the media or generated by spontaneous Raman scattering, when essential gain is provided by maintaining a pump light inside

the media, more photons in the pump light will be converted to Stokes photons, resulting in a stimulated emission process that amplifies the Stokes light.

In optics, SRS provides a mechanism for amplification on specific range in the spectrum. Fiber-based devices like Raman amplifiers and Raman lasers are the applications of SRS which are widely used nowadays. Implementations of such devices on silica waveguide in integrated optics are also reported, exploiting the possibility to realize silicon-based lasers. In super continuum generation, SRS is one of the main factors for long shifting of the spectra from the center frequency. Challenges on improving traditional devices and exploring new phenomenon of SRS remain to be worked on.

### 1.3 Thesis Outline

In this thesis, characteristics of spherical resonators with the dimension of several tens of microns are investigated by simulation and experimental measurement. The fabrication of devices and experiment setups are described in details. The phenomenon of SRS with low threshold input power in silica micro sphere resonators is also demonstrated as one of the applications of micro sphere resonators.

In chapter 2, basic methods and setup of experiment are given. The mathematic models for WGMs and evanescent coupling are deduced. An efficient method for stimulating and coupling WGMs inside the resonator with a tapered fiber is developed. Fabrication of tapered fiber couplers and silica micro spheres are illustrated. Basic experiment setup is shown and resonance-based laser locking technique is introduced.

In chapter 3, a numerical method for solving the modified Helmholtz equation for the mode pattern of WGMs is introduced. Simulation results obtained from the method are presented and indexed by four mode numbers.

In chapter 4, the model for describing the Q-factor of WGM resonators is explained and analyzed. Main factors that are correspondent to the Q-factor of the resonator are listed. Characteristics of silica micro sphere resonators are measured. It is shown that the coupling efficiency can be well controlled by the spatial distance between the tapered fiber and the resonator. Critical coupling situation could also be achieved by this method, which has the most energy confined in the resonator. The degradation of the Q-factor of silica WGM resonators over time is also presented.

In chapter 5, the SRS enhanced by silica micro sphere resonators is observed and the performance is measured and investigated. The reduction in the threshold of SRS in the resonator due to the strong enhancement of the light intensity is observed. In particular, SRS in silica micro sphere resonators is investigated and presents Raman lasers with threshold as low as $1\ mW$.

In chapter 6, chalcogenide glass micro sphere resonators are investigated. The property of chalcogenide glasses is introduced. The fabrication method of micro spheres in chalcogenide glass is developed. Characteristics of chalcogenide glass micro sphere resonators are measured and the potential of adapting these resonators for Raman lasers in mid-infrared band is discussed.

## CHAPTER TWO

## METHODS AND MATERIALS

### 2.1 Mathematical Description of WGM

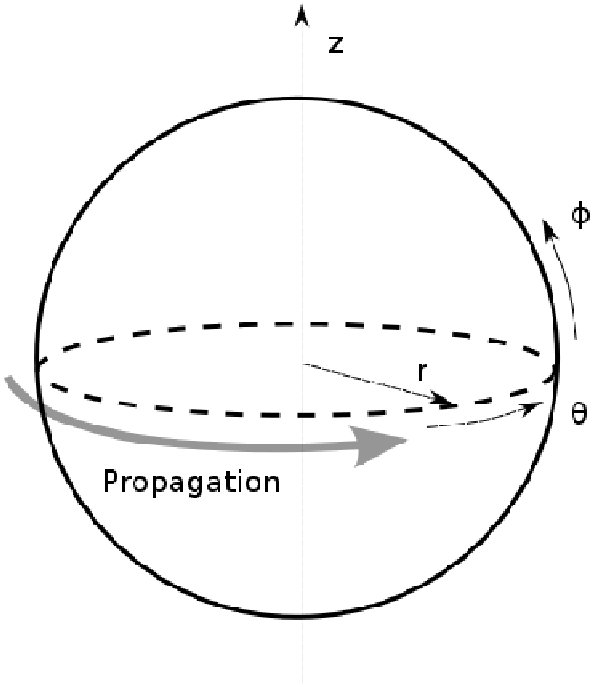


**Figure 2.1.1: WGM propagating direction in spherical coordinates.**

To investigate the mathematical expression for WGMs, we start from the Helmholtz equation which describes the propagating waves:

The modes of light propagating in a dielectric microsphere could be obtained by solving the Helmholtz equation in spherical coordinates:

$$\frac{1}{r^2}\frac{\partial^2}{\partial r^2}(r\psi)+\frac{1}{rsin(\theta)}\frac{\partial}{\partial r}\left(sin(\theta)\frac{\partial}{\partial\theta}\psi\right)+\frac{1}{r^2\,sin^2(\theta)}\frac{\partial^2}{\partial\phi^2}\psi-n^2k^2\psi=0$$

The boundary condition for this structure requires matching Bessel function $j_l(ka)$ and the outgoing Hankel function $h_l(ka)$ at the dielectric boundary. The characteristic equation is given as

$$x\cdot\frac{j_l^{'}(ka)}{j_l(ka)}=\frac{h_l^{'}(ka)}{h_l(ka)}$$

where $x=m$ for TE mode and $x=1/m$ for TM mode.

To obtain the separate field components, assume that the $\phi$ component has the form of

$$\psi_\phi\ =\frac{1}{\sqrt{2\pi}}\,exp(\pm\phi)$$

Equations for other components can be deduced from $\psi_\phi$ and given as

$$\frac{1}{cos(\theta)}\frac{d}{d\theta}(cos(\theta)\frac{d}{d\theta}\psi_\theta)-\frac{m^2}{cos^2(\theta)}\psi_\theta\ \ +l(l+1)\psi_\theta=0$$

$$\frac{d^2}{dr^2}\psi_r+\frac{2}{r}\frac{d}{dr}\psi_r+\left(k^2n(r)^2-\frac{l(l+1)}{r^2}\right)\psi_r=0$$

Equations above have solutions in terms of the generalized Legendre Polynomials $P_m^l(cos(\theta))$, which are commonly written as spherical Harmonics $Y_m^l(\theta)$ and Bessel function$j_l(kr)$.

In details, within the sphere, field component for TE mode is:

$$E_\theta\propto\ -\frac{knm}{sin(\theta)}j_l(knr)Y_l^m(\theta,\phi)$$

And field component for TM mode is:

$$E_r \propto \frac{l(l+1)}{r} j_l(knr) Y_l^m(\theta, \phi)$$

It can be figured out that fields in WGMs are proportional to the product of Bessel function and the spherical harmonics. As the result, WGMs in a microsphere can be identified by four mode numbers, which are the radial mode number$n$, the polar mode number $l$, the azimuthal mode number $m$, and also the polarization number $p$ [12].

Among four mode numbers, $n$ is extracted from the Bessel function and denotes the number of field maxima along the radial direction within the sphere. $l$ and $m$ are values from the spherical harmonics. The value $l$ could be regarded as the number of wavelength enclosed along the equator of the sphere. The value $m$ classifies different components of the spherical harmonics with the same $l$ value, and $|m| \leq l$. $2m$denotes the number of field maxima in the azimuthal path around the equator, and the value $l - m + 1$ is the number of field maxima in the polar direction.

## 2.2 Mathematical Description for Coupling Model

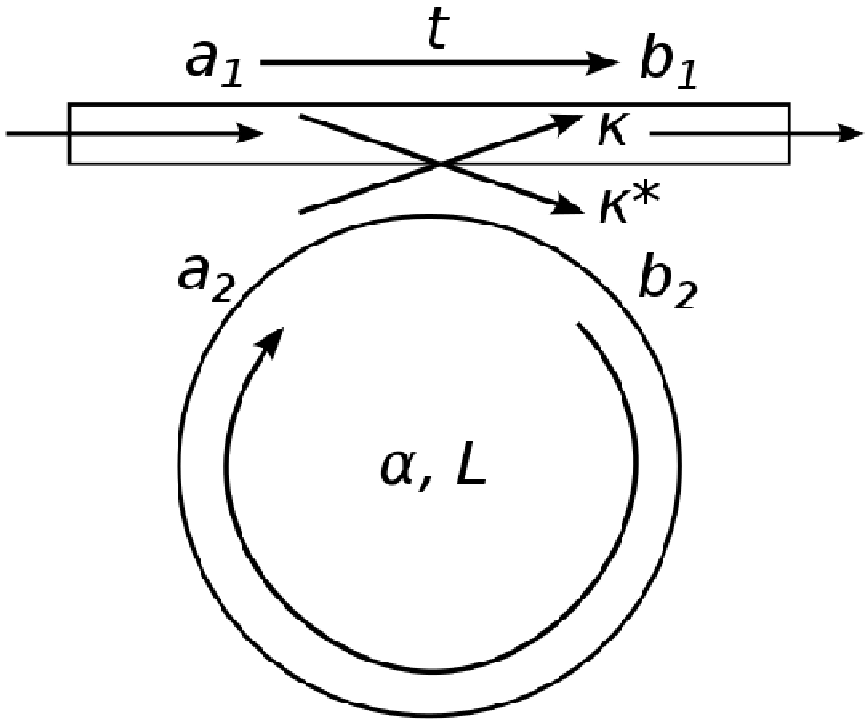


**Figure 2.2.1: Theoretical model for coupling between a waveguide and a resonator.**

Before exploring the properties of WGM resonators, we need to have a good understanding on the theoretical model of the coupling between the waveguide and WGM resonators. Schematic geometry for the coupling mechanism can be regarded as a modified two-port network . As illustrated in Figure 2.1.1, one of the output ports is connected to one of the input ports to represent the resonator, while the rest represents a waveguide passing through [13].

Power exchange between fields in the waveguide and the resonator happens in the coupling region, in which , , , are complex numbers denoting the fields with amplitude and phase. and are the perimeter and attenuation of the resonator.

$t$ and $\kappa$ are the field transmission and coupling coefficients between the waveguide and the resonator in the coupling region. We assume that the system has reached a steady state and there's no reflection or loss in the coupling region. With the assumption, the coupling process can be described by the matrix expression below:

$$\begin{bmatrix} b_1 \\ b_2 \end{bmatrix} = \begin{bmatrix} t & \kappa \\ \kappa^* & -t^* \end{bmatrix} \begin{bmatrix} a_1 \\ a_2 \end{bmatrix}$$

$$|t|^2 + |\kappa|^2 = 1$$

Since the light is circulating inside the resonator,

$$a_2 = b_2 \times \alpha e^{i\theta}$$

where $\theta = \mathrm{n_{eff}L}/\lambda$ is the phase shift in the resonator per cycle, $n_{eff}$ is the effective refractive index of the optical mode, and $\lambda$ is the wavelength.

From equations above, we can solve for the transmission rate from $a_1$ to $b_1$:

$$\frac{|b_1|^2}{|a_1|^2} = \frac{\alpha^2 + |t|^2 - 2\alpha|t|\,cos(\theta)}{1 + \alpha^2|t|^2 - 2\alpha|t|\,cos(\theta)}$$

At resonance, $cos(\theta) = 1$, thus

$$\frac{|b_1|^2}{|a_1|^2} = \frac{(\alpha - |t|)^2}{(1 - \alpha|t|)^2}$$

The equation above indicates that at resonance, the transmission rate is determined by the difference between attenuation $\alpha$ and the coefficient $t$. The system is in under-coupling condition when $\alpha < |t|$, over-coupling condition when $\alpha > |t|$, and critical-coupling condition when $\alpha = |t|$. Details about different coupling conditions will be discussed in chapter 4.

## 2.3 Fabrication of Binocular Tapered Fiber Coupler

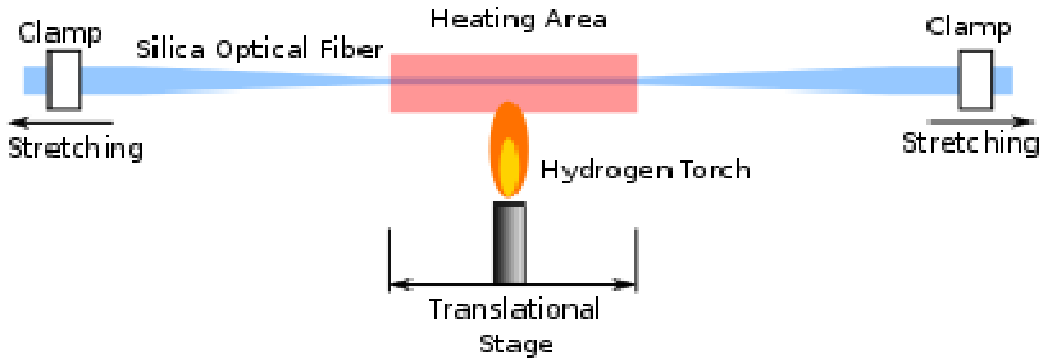


**Figure 2.3.1: Setup for fabricating tapered fiber couplers.**

We use binocular tapered fibers for evanescent coupling in the measurement, which is much more efficient and convenient to implement than other methods such as free-space excitation and prism coupling.

Tapered fibers are fabricated by using a heat-and-stretch process [14, 15]. The schematic illustration for the fabrication setup is shown in Figure 2.3.1. A hydrogen torch is mounted on a translational stage as the heating source, providing high temperature up to to soften the silica without depositing carbon cinders on the fiber. The gas flow in the torch is carefully controlled by a flow meter. Two motorized stages with fiber clamps are placed on each side of the torch for stretching. Figure 2.3.2 is a view for the practical fabrication setup.

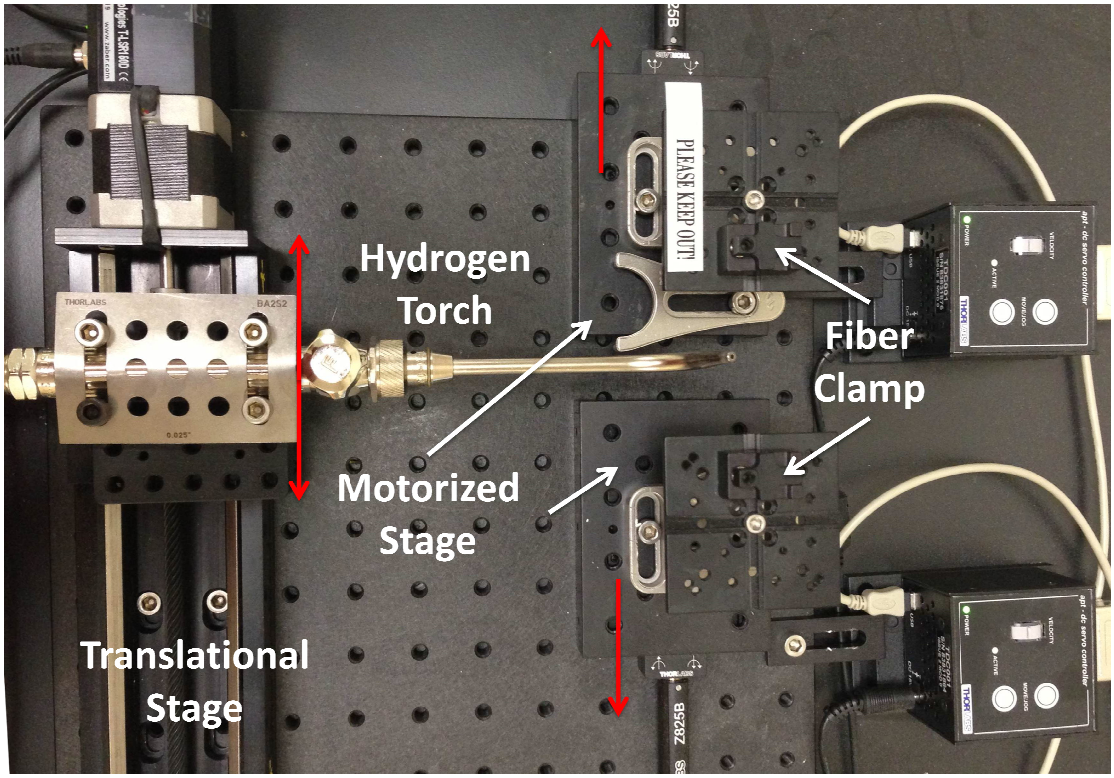


**Figure 2.3.2: Experiment setup for fabricating tapered fiber couplers.**

Single mode fibers (SMF-28) with the diameter of and the core diameter of were tapered in our experiment. The polymer coating was stripped off for the tapering area on the fiber. During fabrication, the fiber was cleaned and mounted over two motorized stages. The fiber was tightened and held by two clamps on both sides. Motorized stages were pulling outward with the torch heating the fiber. The torch also moved back and forth along the fiber in a small distance at the same time to extend the average length of heating region. By using this "flame brush" technique [16], the adiabatic profile for the tapered part of the fiber could be well formed to reduce the total transmission loss of fabricated couplers.

Since essential tension should be maintained on the tapered fiber for mechanical stability during the measurement, the tapered fiber was stretched tight after the heating process had been completed. To transport the tightened fiber to the measurement setup, we then stick the tapered fiber coupler to a U-shaped holder with UV-cured epoxy resin. The tapered fiber was ready to move after the resin had been fully cured by UV light.

The waist of the tapered fiber is about $1\ \mu m$, which can be referred as a silica nano-wire. When light propagates through the coupler, it starts with a confined mode in single mode fiber. Once the light enters the adiabatic region, the diameter of the fiber starts to shrinks, and the mode of light begins to deviate from the original mode and gradually transfer to the wide-spread mode of silica nano-wire. In the waist region, the light is very weakly confined with most of the energy in the evanescent tail outside the nano-wire. When the evanescent tail of the light field overlaps the resonator, which is placed near the tapered fiber, the light will be coupled to the resonator. Since for modes in a nano-wire and a WGM resonator, the propagation constants can be tuned very close, and the wave vectors are parallel, high coupling efficiency can be achieved. As the light passes the waist of the tapered fiber and enters the adiabatic region on the other side, most of the energy can be coupled back to fiber if the profile of the fiber changes slowly enough. Coupling light to WGMs by tapered fiber couplers provides high coupling efficiency and low insertion loss $(\text{less than } 1\text{dB})$, thus is generally used for research works on WGM resonators [17-19].

## 2.4 Fabrication of Silica Micro Sphere Resonators

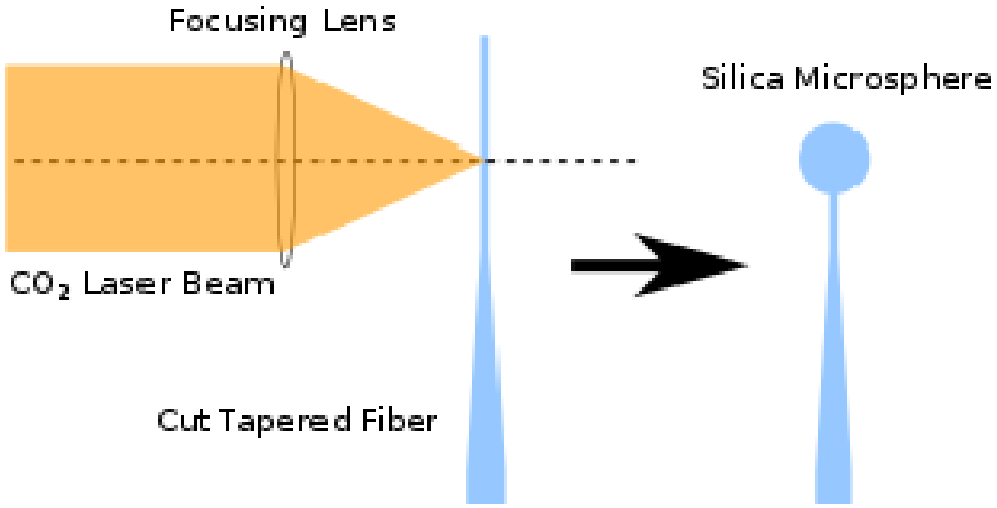


**Figure 2.4.1: Setup for fabricating silica micro sphere resonator using laser.**

Silica is a typical material for making optical communication fibers due to its ultra low attenuation in band. It also shows strong potential for fabricating micro sphere resonators with high Q-factor. The simplest fabrication process is to melt a fiber tip and let it form a sphere by utilizing the surface tension of the material, which is quite intuitive. Since the melting point of silica is as high as , it is necessary to find a proper heating source for fabrication.

One option is the hydrogen flame [20]. The gas flow in the hydrogen torch must be well controlled so that softening temperature of silica is reached and no strong turbulence is introduced, since the turbulence will increase the eccentricity of the sphere. Another approach is to melt the fiber tip by high voltage discharges [21]. The high temperature generated by electrical arcs is used for fiber fusion connection, which also shows the capability for melting the fiber tip. The main problem for this approach is

the uncertainty of the discharging path of the electrical arc. As a result, the size and shape of fabricated spheres are not controllable.

In our setup, we used a focused $CO_2$ laser beam as the heating source [22, 23]. The laser beam with $10.6\ \mu m$ wavelength comes from a $CO_2$ laser with $10\ W$ maximum output power. The beam is focused by a zinc selenide lens ($ZnSe$) with focal length of $5\ cm$. Due to the high intensity of the focused beam and the strong absorption of light near $10.6\ \mu m$ for silica, the fiber can be easily melted near the focal spot.

The fabrication process is fairly straightforward. The fiber is first tapered to proper waist diameters (usually $10\ \mu m$). Then the tapered fiber is cut so that only specific amount of silica will be melted for fabrication. The length of the fiber is calculated according to the estimated volume of the micro sphere. Then the cut tapered fiber is placed near the focal spot of the laser beam. A micro sphere is formed due to the surface tension of melted silica. The fiber is fed into the heating region until expected size of the micro sphere is reached. Rotating the fiber during feeding will help to refine the shape and uniformity of the sphere.

Though the size of micro spheres can be controlled by the length of the silica fiber used for fabrication, the maximum and minimum size of the sphere is limited by several factors. Since the sphere is placed at the end of a tapered fiber, its diameter cannot be smaller than that of the fiber. However, if the diameter of the fiber is less than $10\ \mu m$, it is not able to provide sufficient mechanical support for the micro sphere. Moreover, as the size of the micro sphere approaches the spot size of focused $CO_2$ laser

beam, which is of several hundreds of microns in our setup, it is getting harder to fabricate micro sphere with uniform shape. As the consequence, the diameter of micro spheres is limited from $30\ \mu m$ to $200\ \mu m$ in our fabrication setup.

**Figure 2.4.2: Micro sphere resonator fabricated by $CO_2$ laser.**

In Figure 2.4.2, a photo of a silica micro sphere fabricated by $CO_2$ laser is presented. The diameter of the micro sphere is $74\ \mu m$. The white line in the lower part of the photo is a tapered fiber coupler placed near the sphere. The bright spot in the center of the micro sphere is due to the connection between the sphere and remaining part of the fiber used for fabrication, which is perpendicular to the imaging plane of the photo.

## 2.5 Basic Measurement Setup

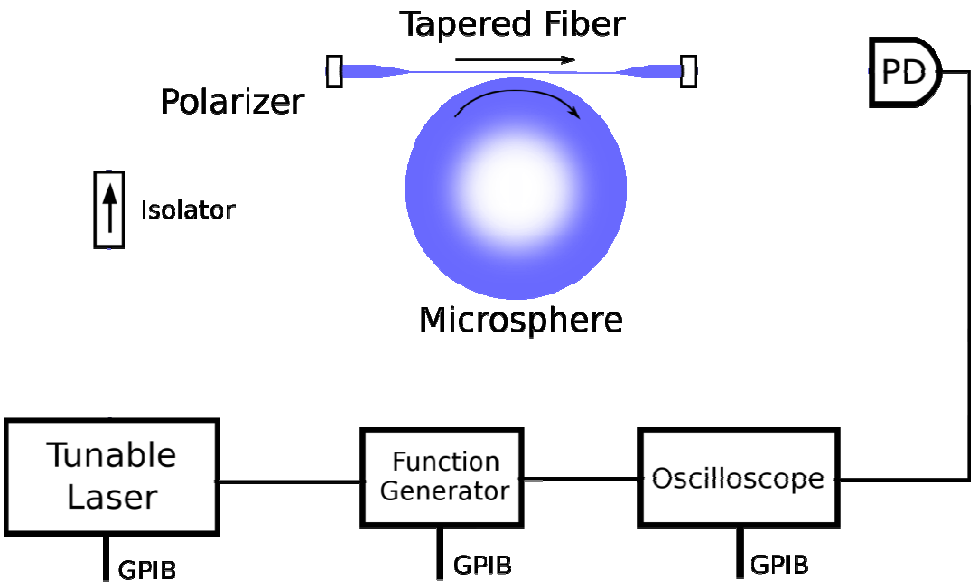


**Figure 2.5.1: Experiment setup for measuring characteristics of micro spheres.**

The basic experiment setup is shown in Figure 2.5.1, which is a fiber-based system. A New Focus Velocity tunable laser operating from 1550 to 1630 nm is adapted as the light source. A function generator is connected to the laser to provide the ramping voltage signal for scanning over the wavelength. To avoid instability induced by the reflection from fiber ends to the cavity of the laser, an isolator is connected to the output port of the laser. Light passes a polarization controller before entering the coupling region of the resonator for selecting WGMs with specific polarization.

Since the coupling condition is extremely sensitive to the distance between the resonator and the tapered fiber, testing environment needs to be as stable as possible,

and positioning of devices should have precision of submicron. The tapered fiber and the micro sphere are placed in an enclosure to isolate the disturbance on device from surrounding air flows. The enclosure is also filled with nitrogen to prevent the degradation of devices when being exposed in the air, which will be explained in chapter 4. The micro sphere under testing is mounted on a motorized stage, which has the ability to move in three dimensions with precision of 50 nm. All the efforts ensure a stable and endurable testing environment for the measurement, so that the transmission spectrum of the resonator could be measured conveniently. Additional components will be added to the basic setup for operating various measurements on the device.

## 2.6 Pound-Drever-Hall Laser Locking Technique

The frequency stability of the laser source is crucial to laboratory usage, especially for measuring optical devices with narrow characteristic line-width. The performance on stability of a laser could be improved if an external cavity is introduced as a reference. By applying an electronic feedback loop to adjust the laser dynamically, the output frequency of the laser could be locked to the resonance of the cavity, providing the same level of stability as the external cavity itself.

A common implementation of the idea is the "Pound-Drever-Hall" (PDH) locking method [24, 25]. It was developed by Ron Drever, R. V. Pound, and Jan Hall in 1983, and is widely used in labs nowadays. PDH locking method provides stability better than 100 Hz, and could be further improved if motion isolation of the cavity is carefully handled.

The key point of applying PDH locking method is to obtain the feedback signal, which can provide a correction on the driving voltage of the piezo actuator in the laser when the frequency of the output light deviates from specific resonance of the external cavity. PDH locking method keeps tracking on the difference between the frequency of the output light and the resonance frequency of the cavity by detecting the deviation of the phase modulated light transmitted through the cavity. This makes PDH technique insensitive to the intensity fluctuation of the laser.

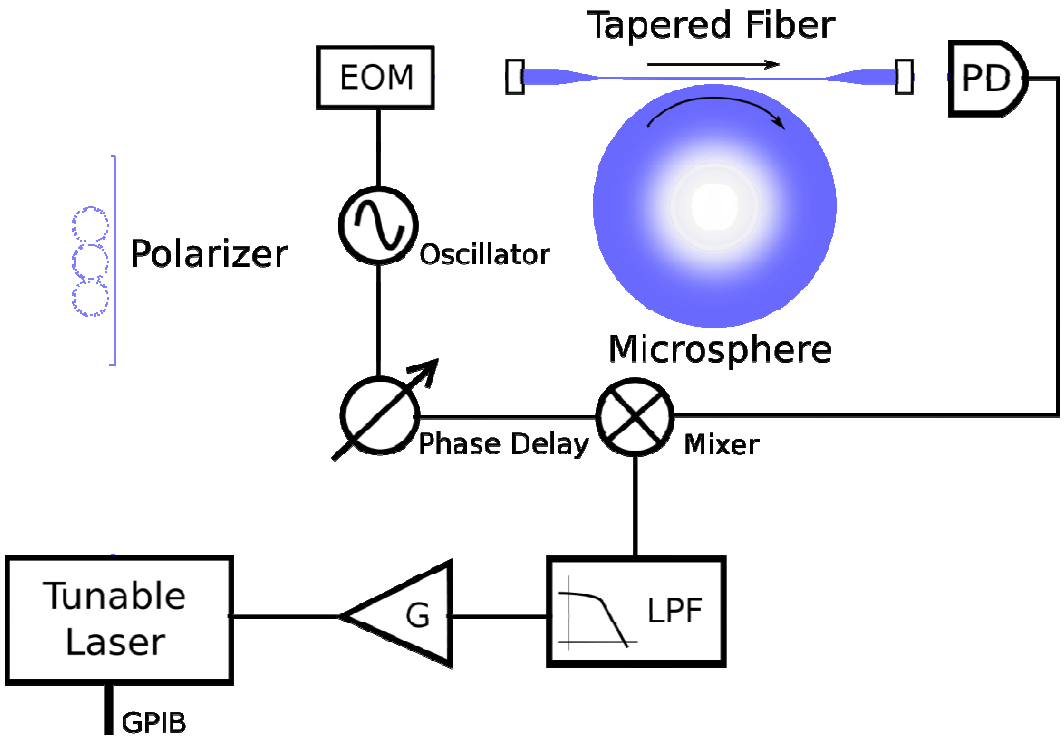


**Figure 2.6.1: Experiment setup for implementing PDH locking.**

Figure 2.6.1 gives details on the implementation of PDH locking technique [26]. Laser light around 1550 nm is first coupled to a standard single mode fiber. The light is modulated by an electro-optic phase modulator (EOM) before entering the coupling

region of the tapered fiber and micro sphere resonator. Transmitted light is collected by a photo receiver. The modulation signal on the EOM is split and delivered to mix with the output of the photo receiver, merging the wanted error signal to low frequencies. After being filtered and amplified, the error signal is fed back to actuate the piezo motor to stabilize the laser frequency.

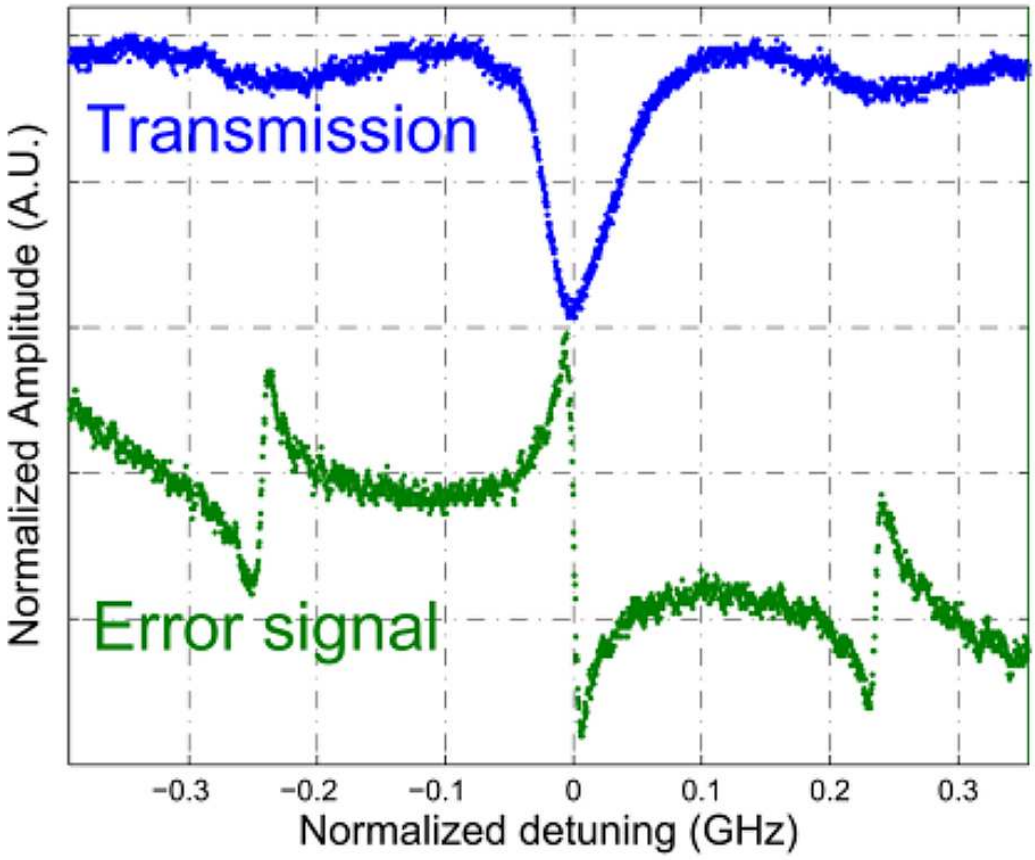


**Figure 2.6.2: Measured error signal near a resonance of a micro sphere.**

Measured error signal from a resonance of a micro sphere is given in Figure 2.6.2. Line-width of the resonance is , corresponding to a total Q-factor of . The linear part of the error signal near the center frequency of the resonance can be

used for the feedback signal on the source laser for stabilization after filtering and amplifying.

## CHAPTER THREE

## SOLVING MODE PATTERNS FOR WGM BY SIMULATION

### 3.1 Numerical Form of Helmholtz Equation

The simulation of WGMs can be implemented by running FEM simulations to solve the weak form of Helmholtz equation [27]. Starting from the Helmholtz equation for magnetic field,

$$\nabla \times (\epsilon^{-1} \nabla \times H) + c^{-2} \frac{\partial^2 H}{\partial t^2} = 0$$

Here, we add a penalty term, $-\alpha\nabla(\nabla \cdot H)$, into the equation to suppress the spurious modes for a better mode preference for the FEM solver:

$$\nabla \times (\epsilon^{-1}\nabla \times H) - \alpha\nabla (\nabla \cdot H) + c^{-2} \frac{\partial^2 H}{\partial t^2} = 0$$

Then we multiply the conjugate of a test magnetic field strength $\widetilde{\mathrm{H}}^*$ and integrate over the dielectric volume:

$$\int_{\mathrm{V}} [(\nabla \times \widetilde{\mathrm{H}}^*) \frac{\cdot}{\epsilon} (\nabla \times \mathrm{H}) - \alpha(\nabla \cdot \widetilde{\mathrm{H}}^*)(\nabla \cdot \mathrm{H}) + \mathrm{c}^{-2}\widetilde{\mathrm{H}}^* \frac{\partial^2 \mathrm{H}}{\partial \mathrm{t}^2}]\mathrm{dV} = 0$$

which is the weak form of Helmholtz equation.

In an axis-symmetric resonator, the magnetic field can be written as

$$H(r) = e^{iM\phi}\{H^r(r,z), iH^\phi(r,z), H^z(r,z)\}$$

and the relative permittivity tensor is diagonal:

$$\epsilon_{diag} = \{\epsilon_{perp}, \epsilon_{perp}, \epsilon_{para}\}$$

in which $\epsilon_{\mathrm{perp}}(\epsilon_{\mathrm{para}})$ is the relative permittivity perpendicular (parallel) to the axis.

Be digging into each weak term, we have:

$$\left(\nabla \times \widetilde{H}^{*}\right)\frac{\cdot}{\epsilon}(\nabla \times H) \;=\; (\frac{A}{r} + B + rC)/(\epsilon_{perp}\epsilon_{para})$$

$$A \;= \epsilon_{perp}\left[\widetilde{H}^{\phi}H^{\phi} \;-\; M\left(\widetilde{H}^{\phi}H^{r} \;+\; H^{\phi}\widetilde{H}^{r}\right) + M^{2}\widetilde{H}^{r}H^{r}\right] + \epsilon_{para}M^{2}\widetilde{H}^{z}H^{z}$$

$$B \;= \epsilon_{perp}\left[\widetilde{H}_{r}^{\phi}\left(H^{\phi} \;-\; MH^{r}\right) + H_{r}^{\phi}\left(\widetilde{H}^{\phi} - M\widetilde{H}^{r}\right)\right] - \epsilon_{para}M(\widetilde{H}^{z}H_{z}^{\phi} \;+\; H^{z}\widetilde{H}_{z}^{\phi})$$

$$C \;= \epsilon_{perp}\widetilde{H}_{r}^{\phi}H_{r}^{\phi} \;+ \epsilon_{para}[(\widetilde{H}_{r}^{z} - \widetilde{H}_{z}^{r})(H_{r}^{z} \;-\; H_{z}^{r}) + \widetilde{H}_{z}^{\phi}H_{z}^{\phi}]$$

$$\alpha(\nabla \cdot \widetilde{H}^{*})(\nabla \cdot H) \;= \alpha\{\frac{D}{r}E + rF\}$$

$$D \;=\; \widetilde{H}^{r}H^{r} \;-\; M(\widetilde{H}^{\phi}H^{r} \;+\; H^{\phi}\widetilde{H}^{r}) \;+\; M^{2}\widetilde{H}^{\phi}H^{\phi}$$

$$E \;=\; (\widetilde{H}_{r}^{r} \;+\; \widetilde{H}_{z}^{z})(H^{r} - MH^{\phi}) + (\widetilde{H}^{r} - M\widetilde{H}^{\phi})(H_{r}^{r} \;+\; H_{z}^{z})$$

$$F \;=\; (\widetilde{H}_{r}^{r} \;+\; \widetilde{H}_{z}^{z})(H_{r}^{r} \;+\; H_{z}^{z})$$

$$\widetilde{H}^{*} \cdot \frac{\partial^{2}H}{\partial t^{2}} \;=\; c^{-2}r(\widetilde{H}^{r}H_{tt}^{r} + \widetilde{H}^{\phi}H_{tt}^{\phi} + \widetilde{H}^{z}H_{tt}^{z})$$

in which $H_{r}^{\phi}$ denotes the partial derivative of $H^{\phi}$ with respect to $r$.

Electric-wall boundary condition is applied for simplicity:

$$H \cdot n = \; 0$$

$$E \times n = \; 0$$

From equations above, boundary condition for magnetic field is given as

$$H^{r}n_{r} \;+\; H^{z}n_{z} \;=\; 0$$

$$H_{z}^{r} \;-\; H_{r}^{z} \;=\; 0$$

By solving the equations above in a FEM solver with defined parameters over the structure, WGMs can be solved and mode patterns will be obtained [28].

### 3.2 Perfect Matched Layer Boundary Condition

Instead of the electric-wall, perfect matched layer (PML), which is an anisotropic absorber, can also be applied as the boundary condition for better precision on results [29]. The permittivity and permeability tensors in PML are given as

$$\bar{\epsilon} = \epsilon\bar{\Lambda}, \qquad \bar{\mu} = \mu\bar{\Lambda}$$

In details, the radial and axial modification factors are given as

$$\bar{\Lambda} = \left(\frac{\bar{r}}{r}\right)\left(\frac{s_z}{s_r}\right)(\hat{r} + \frac{r}{\tilde{r}})(s_z s_r)\hat{\phi} + \left(\frac{\bar{r}}{r}\right)\left(\frac{s_r}{s_z}\right)\hat{z}$$

in which

$$s_r = \begin{cases} n_{medium} & 0 \le r \le r_{pml} \\ n_{medium} - jG\left(\dfrac{r - r_{pml}}{t_{rpml}}\right)^N & r > r_{pml} \end{cases}$$

$$s_z = \begin{cases} n_{medium} - jG\left(\dfrac{z_{lpml} - z}{t_{lpml}}\right)^N & z < z_{lpml} \\ n_{medium} & z_{lpml} \le z \le z_{upml} \\ n_{medium} - jG\left(\dfrac{z - z_{upml}}{t_{upml}}\right)^N & z > z_{upml} \end{cases}$$

$$\hat{r} = \begin{cases} r & 0 \le r \le r_{pml} \\ r - jG\left(\dfrac{(r - r_{pml})^{N+1}}{(N+1)t_{pml}^N}\right) & r > r_{pml} \end{cases}$$

$t_{rpml}$,$t_{lpml}$, $t_{upml}$ and $r_{pml}$, $z_{lpml}$, $z_{upml}$ are the thicknesses and the starting locations of PML in radial, +z and -z directions. $n_{medium}$ is the refractive index of the medium. N is the order of the PML. And G is a positive integer index for optimization.

## 3.3 Results and Discussions

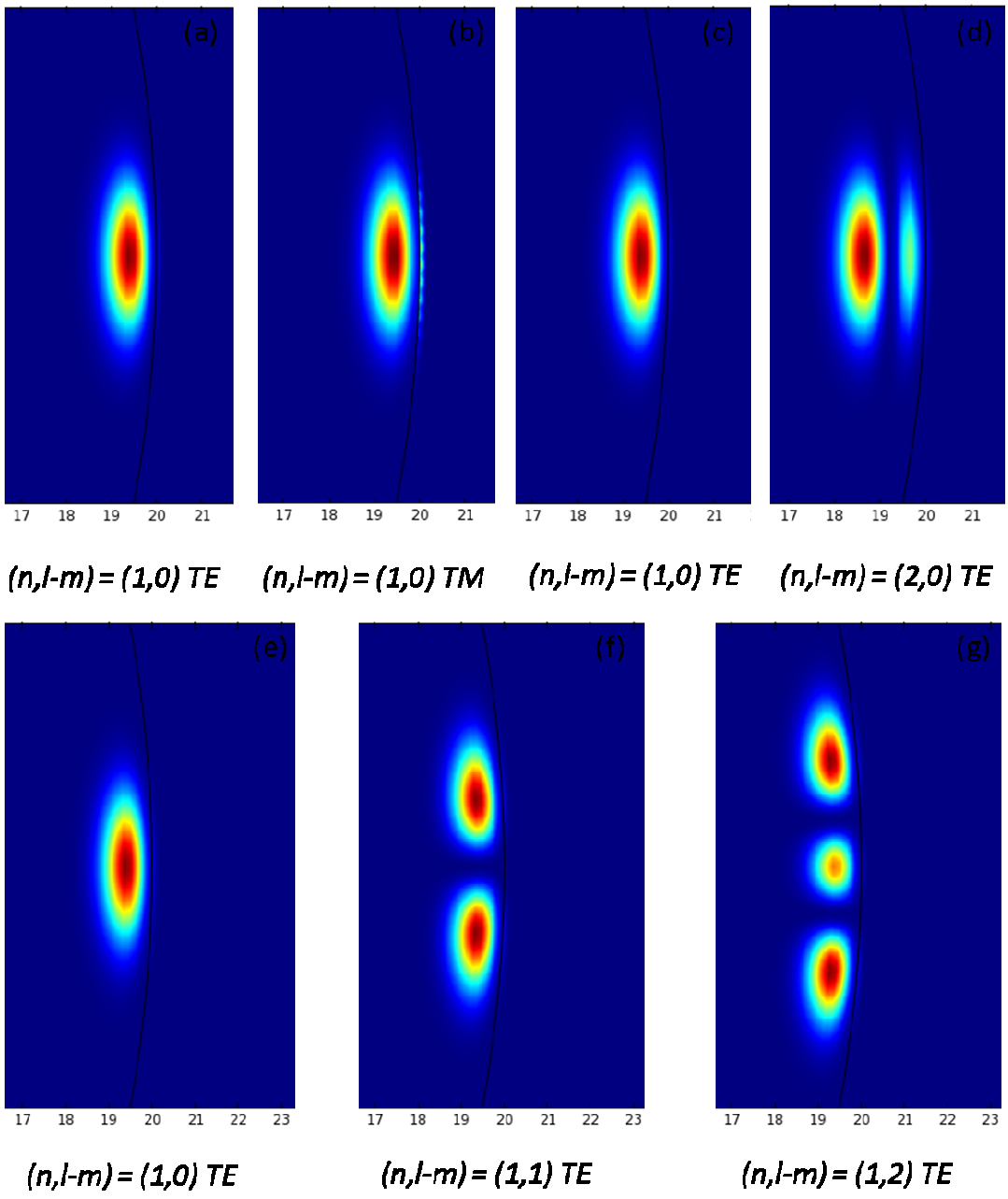


**Figure 3.3.1: Mode patterns of WGMs with various mode numbers from results.**

Results from the simulation are given in Figure 3.3.1. Mode patterns of WGM with different mode numbers are obtained by solving modified Helmholtz Equation in

COMSOL. The radius of the simulated sphere is $20\ \mu\mathrm{m}$ and the refractive index is set to 1.5, which is the typical value for silica. The micro sphere is placed at the center of the simulation area, which is a cubic region filled with air and surrounded by PMLs.

In Figure 3.3.1, WGMs are presented as modes confined near the interface of the sphere by total internal reflection. Although WGMs are not always confined near equator of spherical structure, we are only interested in those not far from the equator since they are more convenient to be excited by current coupling method. In the figure, (a) and (b) show the electric field intensity of two modes with the same mode numbers $(n, l, m)$ but different polarizations. A discontinuity of electric field on the boundary of the sphere is observed in (b) since it is TM polarized. (c) and (d) present two TE modes with different $n$ values. The difference in $n$ leads to different numbers of mode spot in radial direction. (e), (f) and (g) show three TE modes with various $l$ and $m$ values. The difference between $l$ and $m$ is related to the number of spots in polar direction.

With mode patterns from simulation, we are able to calculate the effective mode volume of micro sphere resonators. Maximum and average light intensity over the pattern could be further calculated from simulation results, contributing to the investigation on the performance of resonators that hold WGMs in various optical phenomenon and applications, especially in nonlinear optics where the light intensity is of much importance.

# CHAPTER FOUR

# INVESTIGATION ON CHARACTERISTCS OF SILICA MICRO SPHERE RESONATORS

## 4.1 Spectrum Characteristics of WGM

The free spectrum range (FSR), which is the distance in spectrum between successive azimuthal mode numbers, of WGMs relative to specific cavity can be obtained from the asymptotic solution of Helmholtz equation [30]. When the mode number $l \gg 1$, the FSR could be simplified to:

$$\delta f_{FSR} \approx \frac{c}{2\pi n_m R}\left(\frac{1}{m} - t_n^0 \frac{l^{-2/3}}{3}\right)$$

where $n_m$ is the refractive index of medium, $R$ is the radius of the sphere, $t_n^0$ is the n-th zero of the Airy function, m is the azimuthal mode number and $l$ is the polar mode number.

WGMs can be hold in various spherical structures, like spheres, disks, rings and toroids. Since the micro sphere is a three dimensional structure which has higher degree of degeneracy than other structures, the mode density in micro spheres is also larger. In micro spheres, most modes of our interest are confined near the equator, which have $m$ and $l$ values. However, since the micro sphere measured in the experiment is not perfectly spherical, the degeneracy of $m$ for modes with equal $n$ and $l$ are broken. This leads to clusters of multiple resonances distributed near the center resonance

frequency. The splitting in modes is due to the eccentricity of the spheres and is usually observed when measuring micro sphere resonators.

Starting from the resonant frequencies for perfect spheres, the frequency shift due to eccentricity is given in [23] as below:

$$\frac{\delta f}{f_{(n,l,m)}} = \pm \frac{l^2 - m^2}{4l^2} \epsilon^2$$

in which the eccentricity coefficient $\epsilon = \sqrt{2|r_e - r_a|/r_e}$, $\mathrm{r_e}$ is the equatorial radius, $\mathrm{r_a}$ is the axial radius.

According to the equation above, $\delta f$ depends on the eccentricity coefficient $\epsilon$. Thus the frequency shift between the splitting could be used to evaluate the uniformity of the micro sphere.

### 4.2 Q-factor of Micro Sphere Resonators

The Q-factor is defined as the ratio of the energy stored in the resonator to the energy dissipated per circulation,

$$Q \;=\; 2\pi \times \frac{E_{cav}}{P_{loss}}$$

In a resonator with energy exchange through coupling, the Q-factor consists of the intrinsic part and the external part,

$$Q_{total}^{-1} = Q_0^{-1} + Q_e^{-1}$$

where the intrinsic factor $Q_0$ corresponds to the loss of the resonator, while the external factor $Q_e$ corresponds to the coupling condition.

The intrinsic loss of the resonator can be regarded as a combination of scattering, material absorption and radiative loss, which in mathematics gives the expression for unloaded quality factor $Q_0$:

$$Q_0^{-1} = Q_{sca}^{-1} + Q_{mat}^{-1} + Q_{rad}^{-1}$$

The material absorption limits the ultimate Q-factor of micro sphere resonators of specific materials. The radiative loss depends on the curvature of the surface. As the size of the sphere decreases to the same level of the wavelength, Q-factor will be dominated by radiative loss. For silica micro spheres with radius of tens of microns, the scattering loss is the dominant part for the Q-factor. The refinement of the surface determines the performance of the micro sphere [31, 32].

## 4.3 Results and Discussions

### 4.3.1 Spectral Characteristics

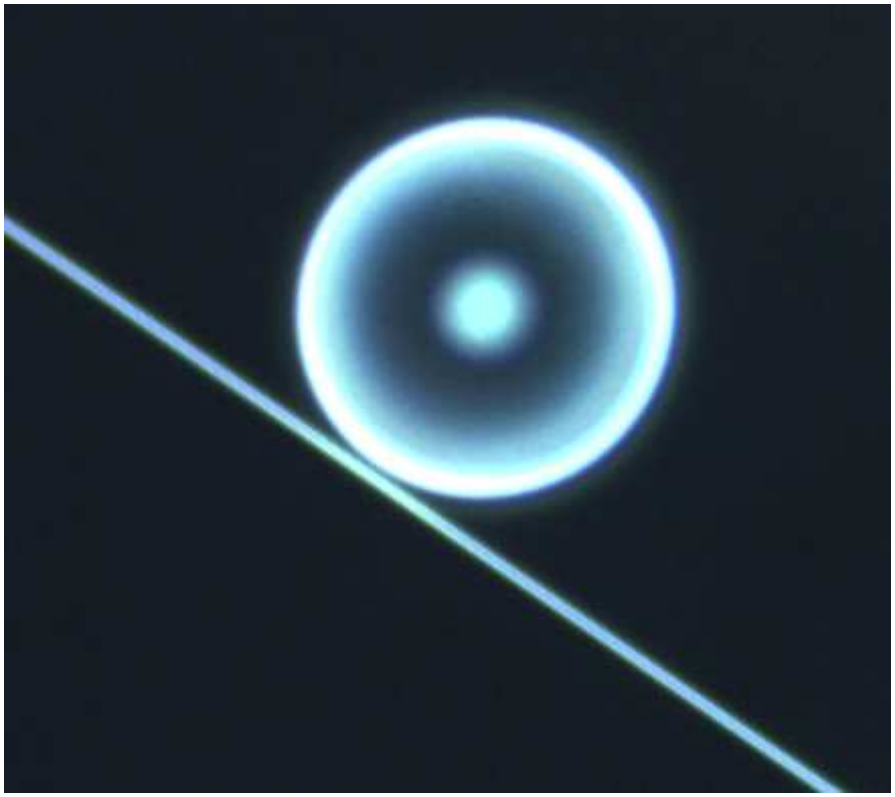

**Figure 4.3.1: Micro sphere coupled to a tapered fiber coupler.**

Due to the large mode density inside the micro sphere resonator, it is tricky to obtain the spectrum of desired sets of modes. To do so, we placed the tapered fiber coupler far from the resonator at the beginning of the measurement, and gradually decreased the distance between the resonator and the tapered fiber coupler with steps of . In every step, we scanned the transmission spectrum of the system from 1540 to . When the coupling was relatively weak, only a small amount of

modes were excited and could be seen on the spectrum, giving us a clean spectrum that could be analyzed and compared to theoretical results.

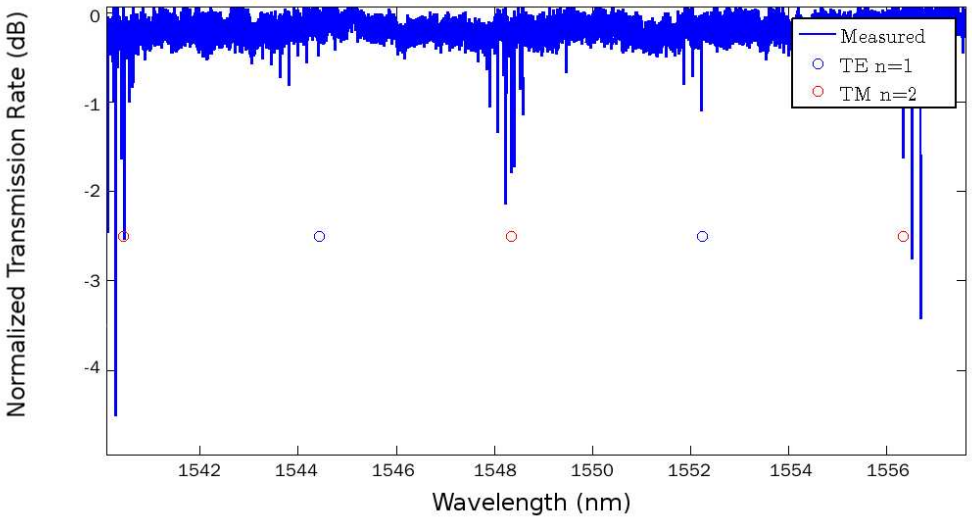


**Figure 4.3.2: Transmission spectrum at weak coupling.**

Figure 4.3.2 shows the transmission spectrum when the tapered fiber coupler was placed from the micro sphere. The radius of the resonator is . The transmission spectrum is normalized to maximum transmitted light intensity. When light was coupled to the resonator, only a portion of input light was received by the detector at the output port. Thus resonance frequencies appeared as dips instead of peaks on the spectrum. The depth of the dip indicates the distinction of light intensity. Both TE and TM modes could be observed on the spectrum, which are two alternately sets of mode clusters. The intensity ratio of TE and TM modes could be precisely controlled by adjusting the polarization controller in the setup. FSR of the TE mode on the spectrum is

, which is identical to theoretical result. Resonant frequencies are also consistent to those from mathematical calculation, which are marked as circles on the figure.

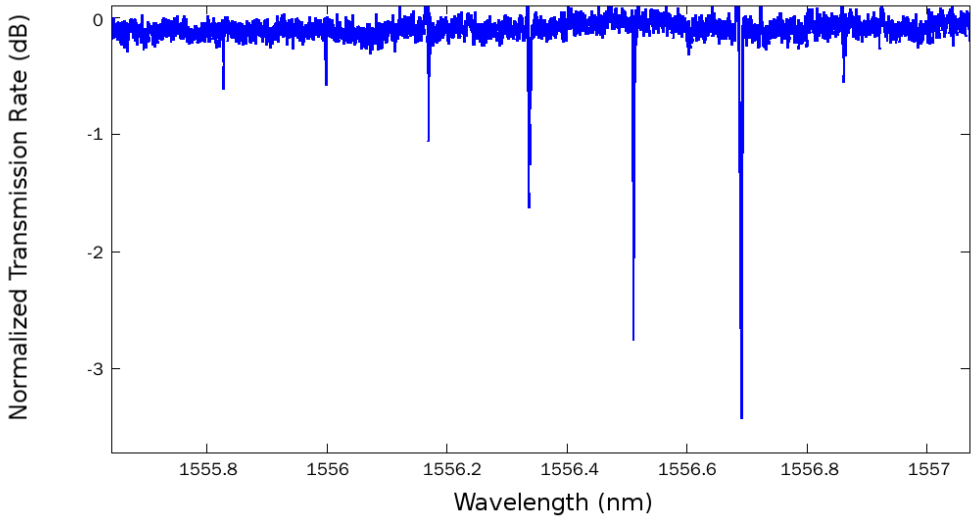


**Figure 4.3.3: Zoom-in view of the transmission spectrum of eccentricity splitting.**

Instead of a single mode at the resonant wavelength, we observed a cluster of modes nearby, as shown in Figure 4.3.3. The mode cluster distributes around the resonance as the center with a constant shift. The phenomenon of resonance splitting is due to the eccentricity of the micro sphere, which causes the degeneracy of modes with different values of mode number at the same frequency. The shift of wavelength, which is in Figure 4.3.3, can be used as a reference to evaluate the uniformity of the sphere.

### 4.3.2 Q-factors in Different Coupling Conditions

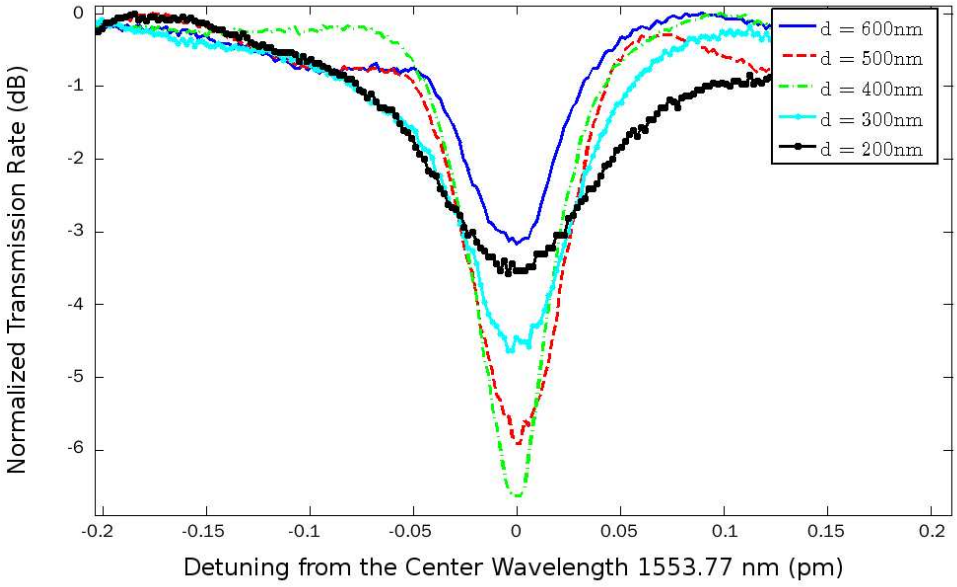


**Figure 4.3.4: Transmission spectrum on a resonance in different coupling conditions.**

According to the coupling model in chapter 2, the on-resonance transmission rate is dependent on the internal loss of the resonator and the coupling condition. When the internal loss is less than the transmission coefficient , it is termed as under-coupling condition, in which only a portion of input light will be coupled into the resonator. When is equal to , the system is in critical-coupling condition and no light will be transmitted to output port. When is larger than , it is over-coupling condition, in which a portion of light in the resonator will be coupled to the output port. With is fixed, as the coupling coefficient increases, the system will experience under-coupling, critical-coupling and over-coupling, with an increasing external loss and a decreasing total Q-factor of the resonator [23, 33].

Figure 4.3.4 demonstrates the transmission spectrum near a single resonance of a micro sphere at $1553.77\ \mathrm{nm}$ with various coupling conditions. The system started with an initial distance of $600\ \mathrm{nm}$ , which leads to weak coupling coefficient and the system was in under-coupling condition. The line-width of the resonance is $0.03\ \mathrm{pm}$, resulting in a total Q-factor of $5.2 \times 10^7$ at $1553.77\ \mathrm{nm}$. As the resonator moved closer to the tapered fiber, the intrinsic Q remained the same while the external Q decreased, presenting a decreasing total Q and expanding line-width on the spectrum. The system transferred from under-coupling to critical-coupling with an increasing distinction rate of the transmitted light first, and then from critical-coupling to over-coupling condition with a decreasing distinction rate. When the distance between the resonator and the tapered fiber reached the minimum value of $200\ \mathrm{nm}$ in the measurement, the Q-factor decreased to $1.4 \times 10^7$. Intrinsic Q-factor of the resonator was calculated according to measured data, which is $9.7 \times 10^7$.

### 4.3.3 Degradation of the Q-factor Over Time

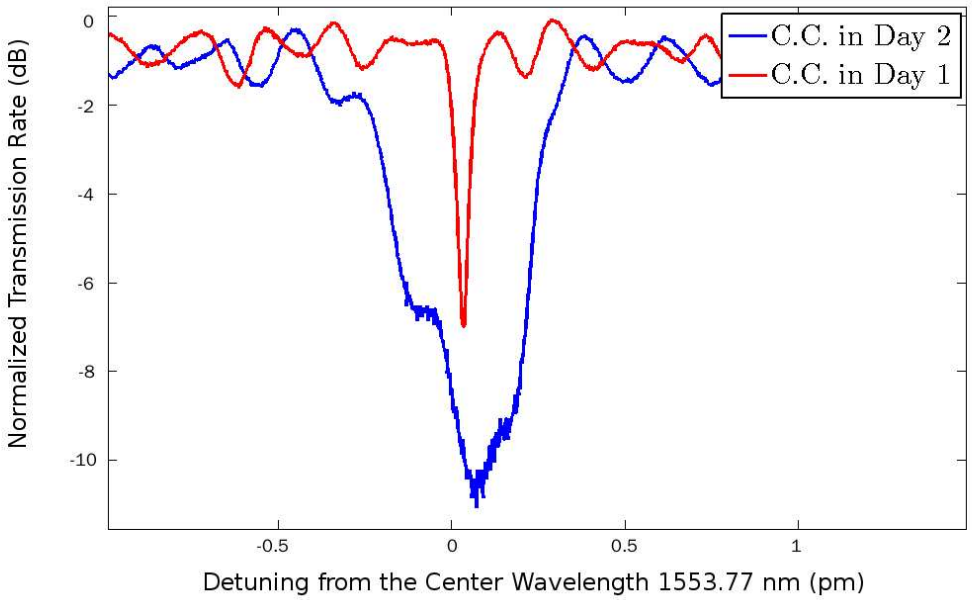


**Figure 4.3.5: Transmission spectrum measured in different time.**

During the measurement, degradation of the performance of silica devices over time is the main problem for the consistency of the device under testing. The transmission rate of the tapered fiber coupler decreased from to in 24 hours after fabrication. Similar degradation on the Q-factor of micro spheres was also observed.

As shown in Figure 4.3.5, a resonance at was measured twice on the same resonator. The resonator was placed in the air and isolated from dusts when it was not mounted on the experiment setup. One of the measurements in red line was operated right after the fabrication of the micro sphere, while another in blue line was operated 24 hours after the fabrication. The Q-factor in the first measurement is near

$1 \times 10^8$, and decreased to $3 \times 10^6$ in the second one, showing a degradation of almost two orders in 24 hours.

The degradation is the consequence of the chemical property of silica. Silica, or silicon dioxide, is regarded to be stable in the air. However, it can be etched by alkalis. When the device is exposed in the lab, it will be gradually etched by $\mathrm{OH}^-$ ions, which come from the ionization of a small portion of $\mathrm{H_2O}$ in the air [34]. The process creates small cracks on surface of the micro sphere and the tapered fiber, which significantly increases the scattering loss when the light propagates along the surface. To prevent the degradation and extend the available usage time, devices should be isolated from the $\mathrm{H_2O}$ in the air, for example, by placing all devices in a nitrogen-filled enclosure during the measurement and keeping them in a sealed dry box with desiccant inside for storage.

## CHAPTER FIVE

## SRS IN SILICA MICRO SPHERE RESONATORS

### 5.1 Resonance-enhanced SRS

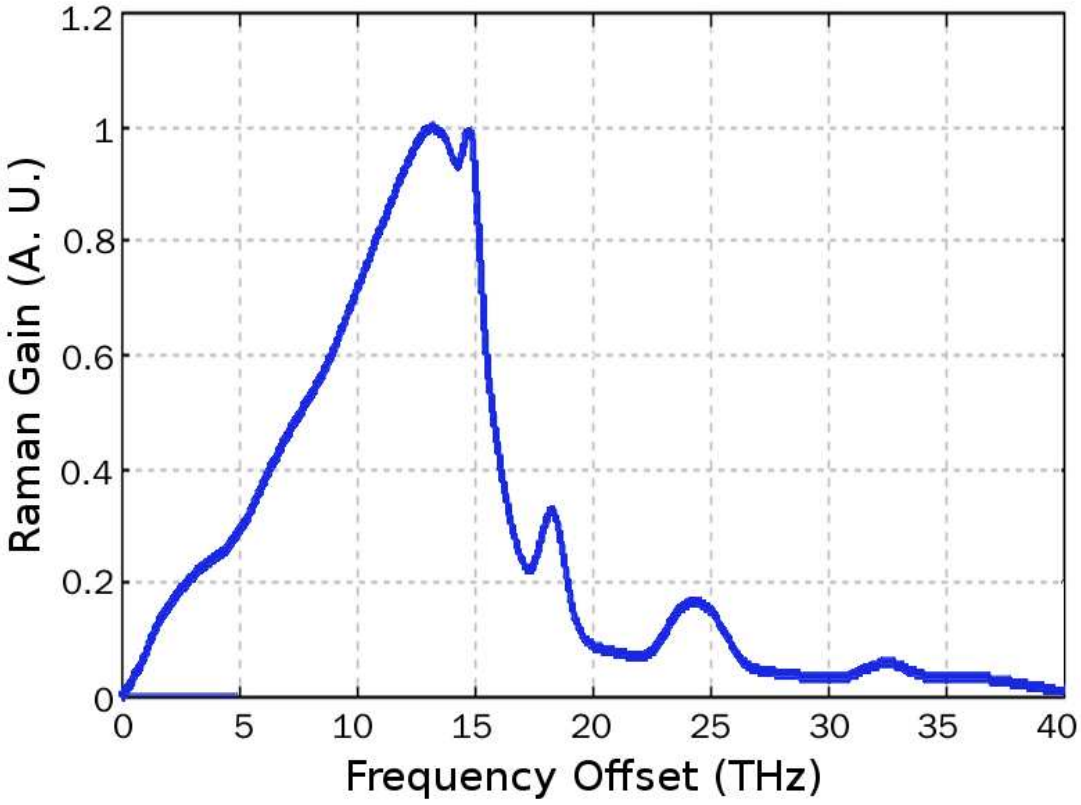


**Figure 5.1.1: Raman gain spectrum of silica.**

Raman gain as a function of the frequency shift is shown in Figure 5.1.1, with the assumption that the pump light and the scattered light are in the same polarization. The line-width of the gain profile is with the peak value shifting away from the pump light [35]. With pump light near , the scattered light from SRS is

expected to be shifted about $112\ \mathrm{nm}$ from the original wavelength and appear around $1662\ \mathrm{nm}$.

Micro sphere resonators with high Q-factors provide a way to confine the light in a structure in microns with long photon life time and compact optical modes (WGMs), which could be utilized to implement resonance-enhanced SRS phenomenon. The most significant potential advantage is the reduction in the size of the device and the threshold input power, which is in hundreds of milliwatts for fiber-based devices [36]. Since in the resonator the SRS involves two different optical modes, one for the pump light and another for the scattered light, it is necessary to define a parameter to indicate the strength of interaction between two modes [37, 38]. We take the effective mode volume as the merit, which is given as:

$$V_{eff} = \frac{\iiint |E_P|^2\, dV \iiint |E_R|^2\, dV}{\iiint |E_P|^2 |E_R|^2\, dV}$$

in which $E_P$ is the electric field of pump light, and $E_R$ is the electric field of scattered light in Raman process. The value of the effective mode volume depends on both the field amplitude and spatial overlap of two modes. The threshold of the input pump light power for resonance-enhanced SRS is given in as:

$$P_t = \frac{1}{C(\Gamma)} \frac{\pi^2 n^2}{g_R \lambda_P \lambda_R} \frac{V_{eff}}{Q_0^2} \frac{(1+K)^3}{K}$$

in which $C(\Gamma)$ is the term correlating to the inter-mode coupling between the clockwise and counterclockwise modes in spherical resonators, $g_R$ is the Raman gain coefficient, $K$ is the coupling coefficient, and $Q_0$ is the unloaded Q-factor of the resonator.

From the equation above, the threshold pump power for resonance-enhanced SRS is relevant to the Q-factor of the resonator. Due to the inverse quadratic relation between the threshold power and the Q-factor, the pump light and scattered light may be enhanced by resonance simultaneously as a result of the large mode density in micro sphere resonators, making it possible to observe SRS with reduced threshold.

## 5.2 Experiment Setup

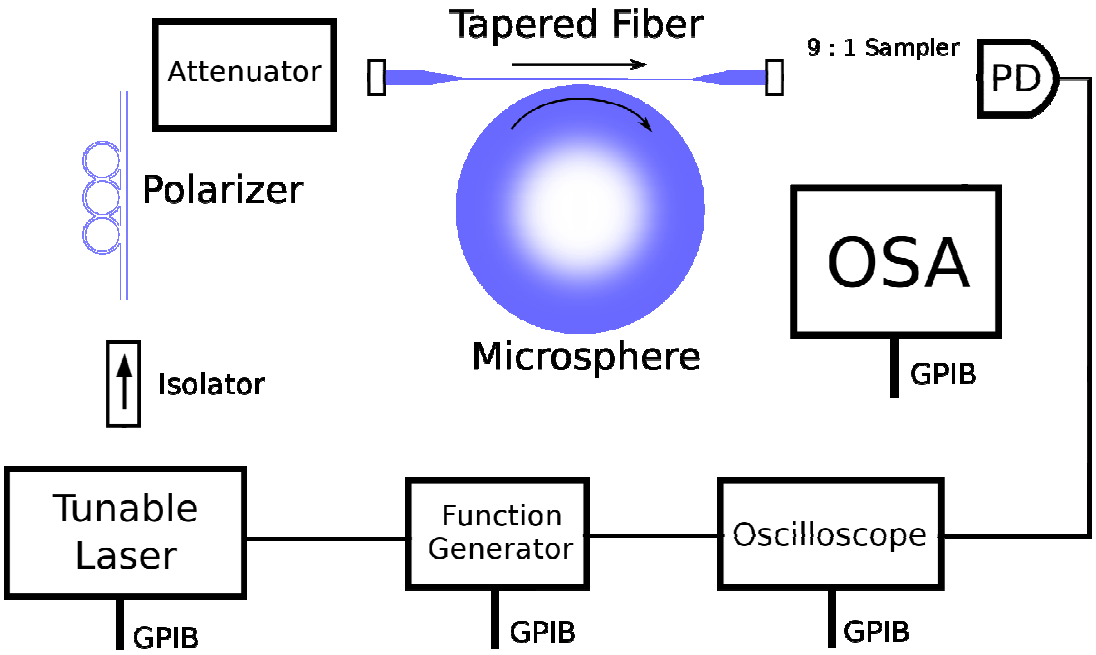


**Figure 5.2.1: Experiment setup for observing SRS in micro sphere resonators.**

To detect the scattered light from SRS, an optical spectrum analyzer (OSA) was added to the setup in Figure 2.5.1. The output light from the tapered fiber coupler was split by a 9:1 sampler, with major portion of the light delivered to the OSA and the rest to the PD for obtaining the transmission spectrum near the resonance, as shown in

Figure 5.2.1. A tunable attenuator was also connected between the polarization controller and the tapered fiber coupler for adjusting the power of the pump light.

Direct DC voltage instead of scanning signal from the function generator will be applied on the piezo motor in the tunable laser when the transmission spectrum had been obtained to adjust the wavelength of the pump light. Scattered light from SRS can be found on the spectrum of OSA when the pump power reached the threshold.

## 5.3 Results and Discussions

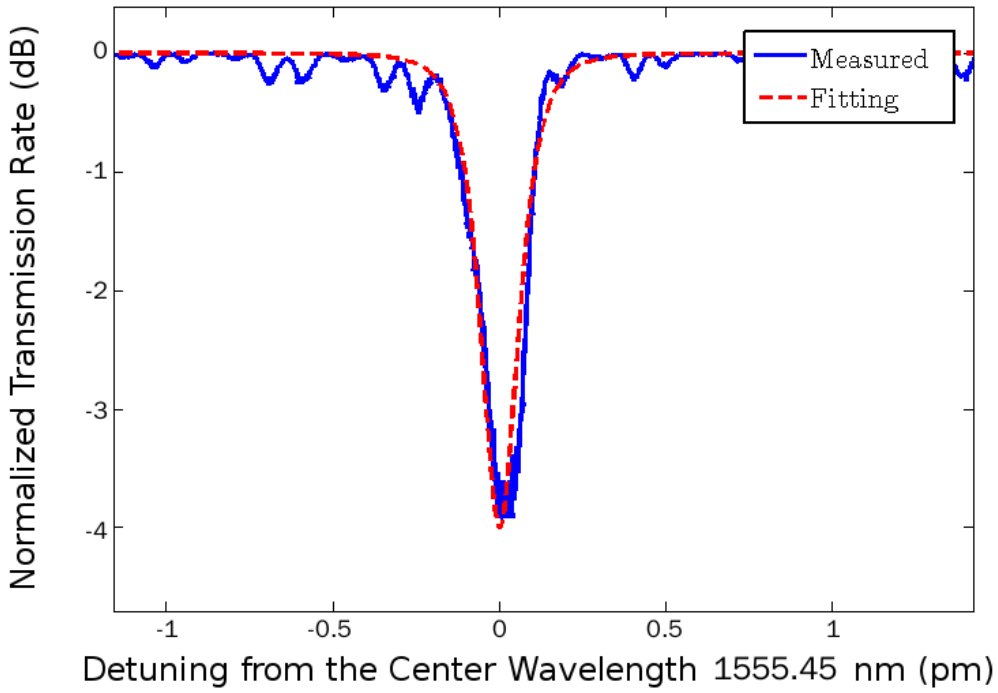


**Figure 5.3.1: Transmission spectrum of a resonance for pump light.**

Measuring process for resonance-enhanced SRS is described as following: The transmission spectrum of the resonator was scanned to select mode with high Q-factor

for dropping pump light. The attenuator was set to high attenuation so that only several microwatts of light were used for scanning to avoid deformation on the obtained resonance spectrum. After the laser had been tuned to the resonance wavelength by adjusting the driving voltage on the piezo motor, the power of pump light would be increased gradually until scattered light appeared on the spectrum. Transmitted pump light and scattered light from the resonator were received by the OSA, presenting an optical spectrum with peaks in several wavelengths. Figure 5.3.1 shows one of the resonance modes used for pump light, which has an unloaded Q-factor of $1 \times 10^8$.

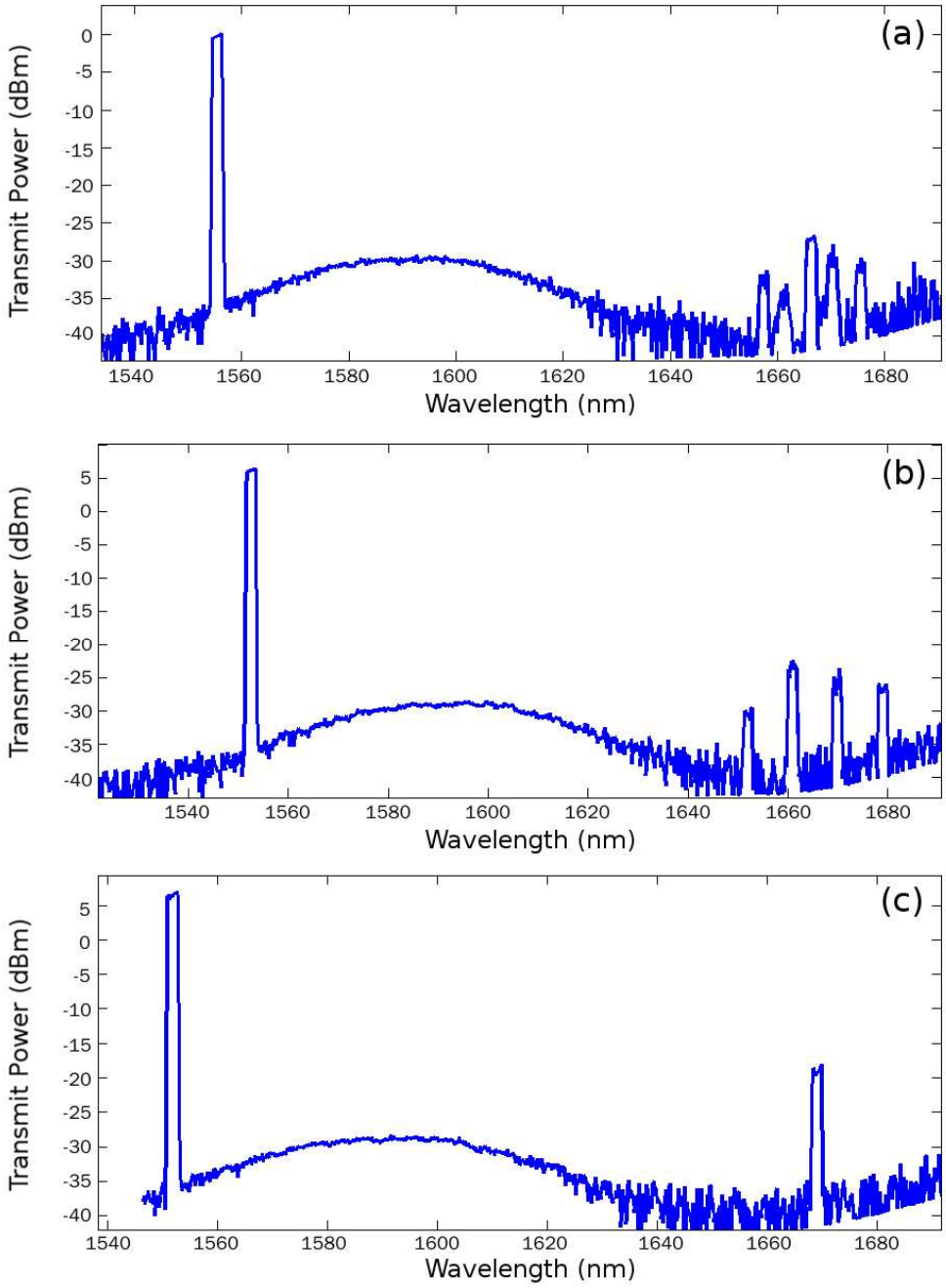


**Figure 5.3.2: Spectrum of transmitted pump light and scattered light from SRS.**

Results from SRS measurement are presented in Figure 5.3.2. The peak near is the transmitted pump light received by OSA. Due to the thermal effect of

silica micro sphere caused by absorption, the resonance position is shifted by the change in refractive index of the material and the portion of the dropped pump power will be capped. In (a), a cluster of modes with amplitude from $-33$ dB to $-26$ dB appear near the center wavelength $1667$ nm. In (b), the phenomenon is similar to (a), but the wavelength shift between excited modes is constant, which is close to the FSR of $9$ nm for TM modes in the resonator. In (c), only a single mode for scattered light is excited. The average Raman shift is $113$ nm with the pump light at $1555$ nm. The lowest threshold for resonance-enhanced SRS was measured to be $1$ mW, which is two orders lower than reported values in fiber-based SRS devices. The average transition rate between the dropped pump power and scattered light power is $5.3\%$.

The quantity of excited scattered light modes varies with the wavelength of the pump light. When pump power is dropped into different resonant modes of the micro sphere, the center wavelength of the Raman gain profile falls into different regions. Due to the large mode density in the micro sphere resonator, all modes with sufficient gain near the peak of Raman gain profile will be excited, presenting a cluster of lasing mode with Raman shift (112 nm) from the wavelength of the pump light.

Bi-stability of the threshold power was also observed. The threshold power could be measured either by increasing the pump light power until scattered light from SRS appeared in the spectrum, or by decreasing the pump light power until the scattered light disappeared. We noticed that results from these two methods were not identical. The threshold measured by increasing the pump light power, which is $4$ mW in our

result, was higher than that by decreasing the pump light power, which is $1\ \mathrm{mW}$. The bi-stability comes from the thermal effect in the resonator due to the absorption of the material and SRS process. Suppose that the resonator starts from low pump power with no SRS happening (referred as the “cold state”), and finally reaches a static state when SRS happens continuously (referred as the “hot state”). Since both the absorption of the material and SRS process will rise the temperature of the resonator, which will also change the refractive index, leading to deformation of mode patterns. The overlapping between mode patterns of pump light and scattered light in hot state is better than that in cold state, resulting in a lower threshold power. When the resonator is switching from cold state to hot state, the only heat source is the absorption, thus it takes more power to start SRS process. When it is switching from hot state to cold state, SRS process will also contribute to heating the resonator and help maintain the overlapping of the pump light and scattered light, therefore resulting in a lower threshold than the former situation.

# CHAPTER SIX

# CHALCOGENIDE GLASS MICRO SPHERE RESONATORS

## 6.1 Chalcogenide Glasses

Chalcogenide glasses are a class of amorphous semiconductor materials containing chalcogen elements from group 6A of the period table, like sulfur, selenium and tellurium. Unique optical properties of chalcogenide glasses have been reported due to covalent bonds between heavy elements in the composition [39]. For example, arsenic tri-sulfide ($As_2S_3$) glass has a high refractive index of 2.4 and a broad transparent window from $2\ \mu m$ to $11\ \mu m$, making it a competitive candidate for optical material in near to mid infrared band. Moreover, $As_2S_3$ glass has Raman gain in the order of $10^{-10}$, which is 3 orders higher than that of silica, and Raman shift of $340\ cm^{-1}$ with line-width of $85\ cm^{-1}$, showing strong potential for providing Raman amplification and lasing in mid infrared band ($2 - 10\ \mu m$).

For the Raman spectrum is usually broad and with a large frequency shift (about $10\ THz$), SRS provides a good option for generating light with frequency that might be difficult to obtain by other approaches, specifically for the mid-infrared band. By combining the advantages of micro sphere resonators and chalcogenide glasses, it is promising to expect Raman amplifier and laser in mid infrared band with reduced pumping threshold. Here we fabricated $As_2S_3$ micro sphere resonator, investigated its properties, and explored the performance it may have.

## 6.2 Fabrication

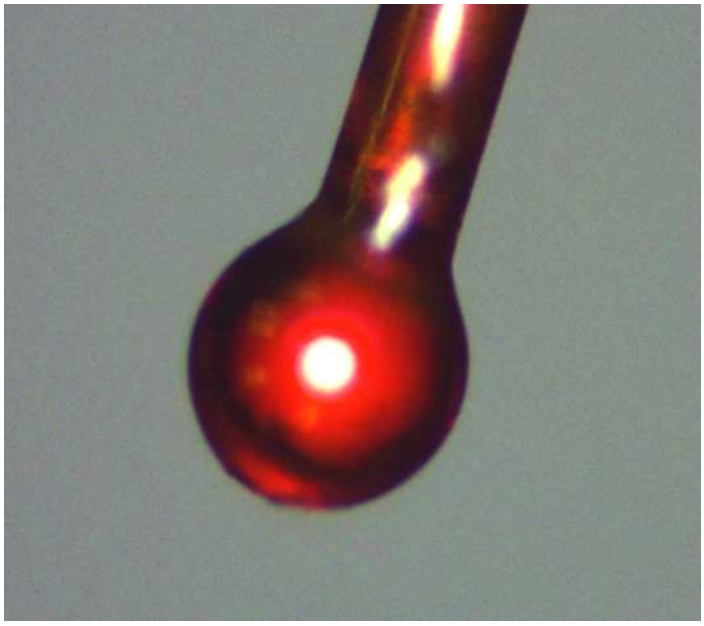

**Figure 6.2.1: $As_2S_3$ micro sphere with the radius of $24.5\ \mu m$.**

The $As_2S_3$ micro sphere can be fabricated by a melting and cooling process similar to that for making silica micro spheres [40, 41]. The main problem for the fabrication is that the melting point of $As_2S_3$ is only $310\ ^\circ C$, and $As_2S_3$ does not have absorption peak near $10.6\ \mu m$ as silica, thus neither hydrogen torch nor focused laser beam from a $CO_2$ laser can be applied as the heating source. As the result, chemical etching method is adapted for tapering and a micro-electro-mechanical-system (MEMS) heater with precise temperature control is used as the heating source for handling $As_2S_3$ glasses.

We started from a piece of $As_2S_3$ fiber with a diameter of $170\ \mu m$. The fiber was first dipped into $1 mmol/ml$ NaOH solution for etching until its diameter had reached $20\ \mu m$. It was then carefully rinsed before being mounted on a three dimensional

optical stage. reacts with the oxygen in the air during the heating process and produces particles on the surface, which will reduce the Q-factor of the fabricated resonator. Thus, the MEMS heater and the stage with etched fiber were kept in an enclosure filled with nitrogen gas during the fabrication process. The tip of the fiber was moved into the heating region and melted in to a sphere. The size of the sphere was monitored by a microscope and could be adjusted by the amount of fiber fed into the heating region. An micro sphere with a radius of by the method described above is shown in Figure 6.1.1.

## 6.3 Results and Discussions

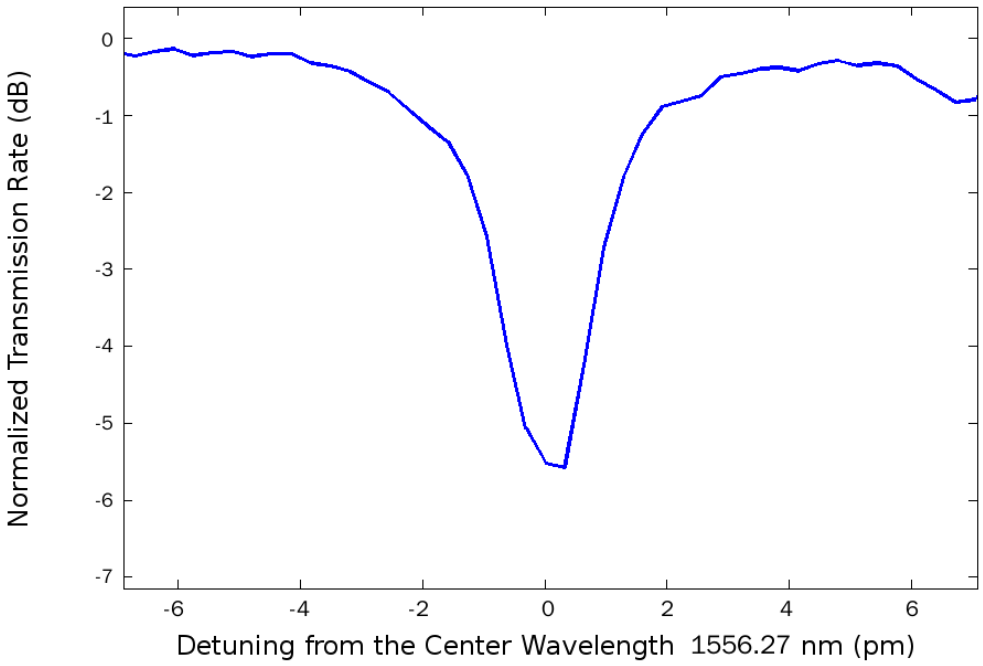


**Figure 6.3.1: Transmission spectrum near for an micro sphere.**

$As_2S_3$ micro sphere resonators were measured with same experiment setup in Figure 5.1.2. The transmission spectrum for a resonance near $1556.27\ \mathrm{nm}$ used for pump light is given in Figure 6.2.1. The line-width of the resonant mode is $2.1\ \mathrm{pm}$, indicating a total Q-factor of $7.2 \times 10^5$. By fitting the data with the coupling model, unloaded Q-factor of $1.4 \times 10^6$ can also be obtained.

According to chapter 5, the threshold for pump light of resonance-enhanced SRS corresponds to the effective mode volume, the Raman gain coefficient and the unloaded Q-factor of the resonator. The threshold of SRS in $As_2S_3$ micro spheres can be estimated based on the measured threshold of silica micro spheres:

$$P_{th}(silica) \propto \frac{V_{eff}}{g_R Q_0}(silica), \qquad P_{th}(silica) \propto \frac{V_{eff}}{g_R Q_0}(silica)$$

$$P_{th}(As_2S_3) = \frac{V_{eff}}{g_R Q_0}(As_2S_3) \times \frac{g_R Q_0}{V_{eff}}(silica) \times P_{th}(silica)$$

By inserting the threshold for silica micro spheres in Chapter 5, which is 1 mW, the unloaded Q-factor of the silica micro sphere ($1 \times 10^8$) and Q-factor of the $As_2S_3$ micro sphere in Figure 6.2.1 ($1.4 \times 10^6$) into the equation above, the estimated threshold of SRS for $As_2S_3$ micro sphere at $1550\ \mathrm{nm}$ is calculated to be $100\ \mathrm{mW}$.

The estimated threshold is not reachable in current experiment setup. However, since the threshold power has an inverse quadratic relation with the Q-factor of the micro sphere, it can be reduced significantly by improving the fabrication process of the $As_2S_3$ micro sphere. Besides the absorption of the material, one main factor that causes the reduction on Q-factor is the darkening property of chalcogenide glasses. When

being exposed to heating source or illuminated by intensive light beam, chalcogenide glasses will be darkened, which means that the refractive index of the exposed part will be changed. Inhomogeneous heating during the fabrication will cause non-uniformity in refractive index of the micro sphere. This will introduce extra scattering loss and thus reduce the Q-factor of the resonator. If a homogeneous heating region is applied in the fabrication, higher Q-factors of $As_2S_3$ micro spheres are expected.

## BIBLIOGRAPHY

[1] L. Rayleigh, "The problem of the whispering gallery," Philos. Mag 20, 1001-1004, 1910.

[2] V.S. Ilchenko, A.B. Matsko. "Optical resonators with whispering-gallery modes-part II: applications," Selected Topics in Quantum Electronics, IEEE Journal of , vol.12, no.1, pp.15,32, Jan.-Feb. 2006.

[3] A. Chiasera, Y. Dumeige, P. Féron, M. Ferrari, Y. Jestin, G. Nunzi Conti, S. Pelli, S. Soria, and G. C. Righini. "Spherical whispering-gallery-mode microresonators," Laser Photon. Rev.4(3), 457–482, 2010.

[4] K. Kosma, G. Zito, K. Schuster, and S. Pissadakis. "Whispering gallery mode microsphere resonator integrated inside a microstructured optical fiber," Optics Letters, Vol. 38, Issue 8, pp. 1301-1303, 2013.

[5] M. Gregor, C. Pyrlik, R. Henze, A. Wicht, A. Peters, Q. Benson. "An alignment-free fiber-coupled microsphere resonator for gas sensing applications," Applied Physics Letters , vol.96, no.23, pp.231102,231102-3, 2010.

[6] R. Riviere, O. Arcizet, A. Schliesser, T.J. Kippenberg. "Evanescent straight tapered-fiber coupling of ultra-high Q optomechanical micro-resonators in a low-vibration helium-4 exchange-gas cryostat," Review of Scientific Instruments , vol.84, no.4, pp.043108,043108-7, 2013.

[7] S.I. Shopova, R. Rajmangal, S. Holler, S. Arnold. "Plasmonic enhancement of a whispering-gallery-mode biosensor for single nanoparticle detection," Applied Physics Letters , vol.98, no.24, pp.243104,243104-3, 2011.

[8] B. Peng, S.K. Ozdemir, J. Zhu, and L. Yang. "Photonic molecules formed by coupled hybrid resonators," Optics Letters, Vol. 37, Issue 16, pp. 3435-3437, 2012.

[9] C.V. Raman. "A new radiation," Indian J. Phys. 2: 387–398, 1928.

[10] A. Smekal. "Zur Quantentheorie der Dispersion," Naturwissenschaften, 11, (43), 873-875, 1923.

[11] G. Landsberg, L. Mandelstam. "Eine neue Erscheinung bei der Lichtzerstreuung in Krystallen," Naturwissenschaften, 16, (28), 557, 1928.

[12] A.N. Oraevsky. "Whispering-gallery waves," Quantum Electron, 32, 377-400, 2002.

[13] A. Yariv. "Universal relations for coupling of optical power between microresonators and dielectric waveguides," Electronics Letters, 36(11):321, 2000.

[14] G. Brambilla. "Optical fibre nanowires and microwires: A review," J. Opt., vol. 12, pp.043001, 2010.

[15] S. Xue, M.A. van Eijkelenborg, G.W. Barton, P. Hambley. "Theoretical, Numerical, and Experimental Analysis of Optical Fiber Tapering," Lightwave Technology, Journal of , vol.25, no.5, pp.1169-1176, 2007.

[16] G. Brambilla, F. Xu, P. Horak, Y. Jung, F. Koizumi, N.P. Sessions, E. Koukharenko, X. Feng, G.S. Murugan, J.S. Wilkinson, and D.J. Richardson. "Optical fiber nanowires and

microwires: fabrication and applications," Adv. Opt. Photon., Vol. 1, Iss. 1, pp. 107-161, 2009.

[17] C. Huang, J. Fan, R. Zhang, L. Zhu. "Internal frequency mixing in a single optomechanical resonator," Applied Physics Letters , vol.101, no.23, pp.231112,231112-4, 2012.

[18] J. C. Knight, G. Cheung, F. Jacques, and T. A. Birks. "Phase-matched excitation of whispering-gallery-mode resonances by a fiber taper," Optics Letters, Vol. 22, Issue 15, pp. 1129-1131, 1997.

[19] A.B. Matsko, A.A Savchenkov, D. Strekalov, V.S. Ilchenko, and L. Maleki. "Review of applications of whispering-gallery mode resonators in photonics
and nonlinear optics," IPN Progress Report, 42-162, 2005.

[20] D. W. Vernooy, V. S. Ilchenko, H. Mabuchi, E. W. Streed, and H. J. Kimble. "High-Q measurements of fused-silica microspheres in the near infrared," Optics Letters, Vol. 23, Issue 4, pp. 247-249, 1998

[21] J.P. Laine. "Design and applications of optical microsphere resonators," Helsinki University of Technology, 2003.

[22] L. Collot, V. Lefèvre-Seguin, M. Brune, J.-M. Raimond, and S. Haroche. “Very high-Q whispering gallery modes resonances observed on fused silica microspheres,” Europhys. Lett. 23, 327-333, 1993.

[23] M. Cai, O. Painter, and K. J. Vahala. "Observation of critical coupling in a fiber taper to a silica-microsphere whispering-gallery mode system," Physical Review Letters, 85(1):74-77, 2000.

[24] R.W.P. Drever. "Laser phase and frequency stabilization using an optical resonator", Appl. Phys. B, vol. 31, pp.97-105, 1983.

[25] E.D.Black. "An introduction to Pound–Drever–Hall laser frequency stabilization," Amer. J. Phys., vol. 69, pp.79-87, 2001.

[26] A. A. Savchenkov, A. B. Matsko, V.S. Ilchenko, N. Yu, and L. Maleki. "Whispering-gallery-mode resonators as frequency references. ii. stabilization," J. Opt. Soc. Am. B, vol. 24, no. 12, pp. 2988-2997, 2007.

[27] M. Oxborrow, "Traceable 2-D Finite-Element Simulation of the Whispering-Gallery Modes of Axisymmetric Electromagnetic Resonators," IEEE Trans. Microw. Theory Techniques 55, 1209, 2007.

[28] M. Oxborrow. How to simulate the whispering-gallery modes of dielectric microresonators in FEMLAB/COMSOL", Proc. SPIE 6452, Laser Resonators and Beam Control IX, 64520J, 2007.

[29] M. Imran Cheema and Andrew G. Kirk. "Accurate determination of the quality factor of axisymmetric resonators by use of a perfectly matched layer," arXiv:1101.1984v4, 2012.

[30] A.B. Matsko, V.S. Ilchenko. "Optical resonators with whispering-gallery modes-part I: basics," Selected Topics in Quantum Electronics, IEEE Journal of , vol.12, no.1, pp.3,14, 2006.

[31] M. L. Gorodetsky, A. A. Savchenkov, and V. S. Ilchenko. "Ultimate Q of optical microsphere resonators," Opt. Lett. 21, 453-455, 1996.

[32] K.J. Vahala, "Optical microcavities," Nature 424, 839-846, 2003.

[33] T.J. Kippenberg, S. M. Spillane, and K. J. Vahala. "Modal coupling in traveling-wave resonators," Optics Letters, 27(19):1669-1671, 2002.

[34] Y.Z. Yan, C.L. Zou, S.B. Yan, F.W. Sun, Z. Ji, J. Liu, Y.G. Zhang, L. Wang, C.Y. Xue, W.D. Zhang, Z.F. Han, and J.J. Xiong. "Packaged silica microsphere-taper coupling system for robust thermal sensing application," Opt. Express 19, 5753, 2011.

[35] R. H. Stolen, C. Lee, and R. K. Jain. "Development of the stimulated Raman spectrum in single-mode silica fibers," JOSA B, Vol. 1, Issue 4, pp. 652-657, 1984.

[36] E.M. Dianov, "Advances in Raman fibers," Journal of Lightwave Technology, Vol. 20, Issue 8, pp. 1457-1462, 2002.

[37] H. B. Lin and A. J. Campillo, "Microcavity enhanced raman gain," Optics Communications, 133(1-6):287-292, 1997.

[38] S. M. Spillane, T. J. Kippenberg, and K. J. Vahala. "Ultralow-threshold raman laser using a spherical dielectric microcavity," Nature, 415(6872):621-623, 2002.

[39] B. J. Eggleton, B. Luther-Davies, and K. Richardson, “Chalcogenide photonics,” Nat. Photonics 5, 141–148, 2011.

[40] P. Wang, S. M. Ganapathy, G. Brambilla, M. Ding, Y. Semenova, Q. Wu, G. Farrell. "Chalcogenide Microsphere Fabricated From Fiber Tapers Using Contact With a High-Temperature Ceramic Surface," Photonics Technology Letters, IEEE , vol.24, no.13, pp.1103-1105, 2012.

[41] P. Wang, M. Ding, T. Lee, G. Senthil Murugan, L. Bo, Y. Semenova, Q. Wu, D. Hewak, G. Brambilla, G. Farrell. "Packaged chalcogenide microsphere resonator with high Q-factor," Applied Physics Letters , vol.102, no.13, pp.131110,131110-5, 2013.